Broad-line Type Ic supernova SN 2014ad

D. K. Sahu,[1]★ G. C. Anupama,[1] N. K. Chakradhari,[2] S. Srivastav,[1] Masaomi Tanaka,[3] Keiichi Maeda[4] and Ken'ichi Nomoto[5]†

[1]*Indian Institute of Astrophysics, II Block Koramangala, Bangalore 560034, India*
[2]*Pandit Ravishankar Shukla University, Raipur 492010, India*
[3]*National Astronomical Observatory Japan, Mitaka, Tokyo 181-8588, Japan*
[4]*Department of Astronomy, Kyoto University, Kitashirakawa-Oiwake-cho, Sakyo-ku, Kyoto 606-8502, Japan*
[5]*Kavli Institute for the Physics and Mathematics of the Universe, WPI, University of Tokyo, Kashiwa, Chiba 277-8583, Japan*

ABSTRACT

We present optical and ultraviolet photometry and low-resolution optical spectroscopy of the broad-line Type Ic supernova SN 2014ad in the galaxy PGC 37625 (Mrk 1309), covering the evolution of the supernova during -5 to $+87$ d with respect to the date of maximum in the B band. A late-phase spectrum obtained at $+340$ d is also presented. With an absolute V-band magnitude at peak of $M_V = -18.86 \pm 0.23$ mag, SN 2014ad is fainter than supernovae associated with gamma ray bursts (GRBs), and brighter than most of the normal and broad-line Type Ic supernovae without an associated GRB. The spectral evolution indicates that the expansion velocity of the ejecta, as measured using the Si II line, is as high as $\sim 33\,500$ km s^{-1} around maximum, while during the post-maximum phase it settles at $\sim 15\,000$ km s^{-1}. The expansion velocity of SN 2014ad is higher than that of all other well-observed broad-line Type Ic supernovae except for the GRB-associated SN 2010bh. The explosion parameters, determined by applying Arnett's analytical light-curve model to the observed bolometric light-curve, indicate that it was an energetic explosion with a kinetic energy of $\sim (1 \pm 0.3) \times 10^{52}$ erg and a total ejected mass of $\sim (3.3 \pm 0.8)\,M_\odot$, and that $\sim 0.24\,M_\odot$ of ^{56}Ni was synthesized in the explosion. The metallicity of the host galaxy near the supernova region is estimated to be $\sim 0.5\,Z_\odot$.

Key words: techniques: photometric – techniques: spectroscopic – supernovae: general – supernovae: individual: SN 2014ad – galaxies: individual: Mrk 1309.

1 INTRODUCTION

Core-collapse supernovae arising from progenitors that are stripped of hydrogen and/or helium are known as stripped-envelope supernovae. This includes Types IIb, Ib and Ic supernovae (SNe). For Type IIb SNe, the progenitor retains a thin layer of hydrogen at the time of explosion, whereas in Type Ib SNe, the hydrogen envelope is completely removed. Type Ic SNe show neither hydrogen nor helium in their spectra around maximum brightness, indicating that both the hydrogen and the helium envelope of the progenitor star are removed before the explosion (Filippenko 1997; Turatto 2003). The exact nature of the progenitors and the process operational in removing the outer envelopes are not fully understood. The progenitors of Type Ic SNe are thought to be either massive Wolf–Rayet (WR) stars, or less massive stars in a binary system. In the case of WR stars, the helium envelope is removed by powerful stellar

winds, and in a binary system, mass transfer to the companion helps in the removal of the helium envelope (see Langer 2012 for a recent review).

A small fraction (~ 4 per cent; Shivvers et al. 2017) of Type Ic SNe show very broad lines in their spectra obtained close to maximum light, indicating a very high expansion velocity ($\sim 15\,000$–$30\,000$ km s^{-1}) of the ejecta. These are known as broad-line Type Ic SNe. The association of the GRB 980425 (Galama et al. 1998) with SN 1998bw indicated that GRB-associated SNe are of broad-line Ic type. This was later confirmed by the subsequent discovery of many other broad-line SNe associated with GRBs/X-ray flashes (XRFs) (Hjorth et al. 2003; Stanek et al. 2003; Malesani et al. 2004; Pian et al. 2006; Bufano et al. 2012; Toy et al. 2016). Broad-line Type Ic SNe associated with GRBs/XRFs are also known as engine-driven SNe. They have a rapidly rotating central compact object powered by accretion, and are often associated with relativistic outflow. However, there are some broad-line SNe that are not associated with GRBs/XRFs (Sanders et al. 2012; Mazzali et al. 2013; Walker et al. 2014). A possible interpretation of the absence of an observed GRB for some broad-line Type Ic SNe is a relativistic jet that is initially

Table 1. Magnitudes of secondary standard stars in the field of SN 2014ad. The stars are marked in Fig. 1.

ID	U	B	V	R	I
1	15.559 ± 0.023	15.160 ± 0.015	14.370 ± 0.017	13.895 ± 0.022	13.464 ± 0.016
2	15.194 ± 0.016	15.009 ± 0.020	14.356 ± 0.004	13.963 ± 0.016	13.607 ± 0.009
3	15.717 ± 0.021	15.544 ± 0.022	14.863 ± 0.008	14.458 ± 0.029	14.072 ± 0.025
4	16.078 ± 0.016	15.759 ± 0.018	15.021 ± 0.014	14.590 ± 0.014	14.196 ± 0.017
5	15.271 ± 0.007	15.387 ± 0.017	14.838 ± 0.005	14.463 ± 0.006	14.076 ± 0.018
6	16.319 ± 0.031	15.891 ± 0.014	15.116 ± 0.013	14.672 ± 0.018	14.264 ± 0.015
7	16.918 ± 0.016	16.438 ± 0.017	15.534 ± 0.015	15.019 ± 0.022	14.524 ± 0.017
8	16.008 ± 0.033	15.928 ± 0.012	15.298 ± 0.012	14.920 ± 0.009	14.542 ± 0.012
9	19.799 ± 0.099	18.573 ± 0.003	17.051 ± 0.024	16.003 ± 0.011	14.850 ± 0.013
10	16.746 ± 0.020	16.228 ± 0.027	15.421 ± 0.005	14.925 ± 0.004	14.481 ± 0.023
11	16.651 ± 0.009	16.438 ± 0.022	15.749 ± 0.006	15.338 ± 0.018	14.954 ± 0.022
12	16.739 ± 0.034	16.829 ± 0.015	16.290 ± 0.030	15.944 ± 0.034	15.611 ± 0.034
13	14.951 ± 0.033	15.145 ± 0.002	14.839 ± 0.005	14.630 ± 0.012	14.379 ± 0.012

beamed away from the line of sight of the observer (Rhoads 1999). As the decelerating jet spreads laterally, the emission becomes effectively isotropic and shifts to longer wavelengths. Irrespective of the initial viewing angle, the afterglow emission in the radio is expected to increase rapidly on a time-scale of a few weeks to several years (Perna & Loeb 1998; Waxman 2004). Thus late-phase observations in the radio can be used to search for evidence of off-axis GRBs (Soderberg et al. 2006, and references therein). The non-detection of late-time radio emission from a sample of Type Ibc SNe, including broad-line Type Ic SNe, led Soderberg et al. (2006) to conclude that not every broad-line Type Ic SN harbours a GRB.

In a systematic study by Modjaz et al. (2016), it was shown that Type Ic SNe with GRBs have higher expansion velocities as well as broader line widths than Type Ic SNe without an observed GRB. Based on this, it was suggested that the broad-line Type Ic SNe without an observed GRB may have had lower energy and/or a choked jet that imparted lower velocities to the supernova ejecta. Recently, two energetic broad-line Type Ic SNe, namely 2009bb (Pignata et al. 2011) and 2012ap (Milisavljevic et al. 2015), showed mildly relativistic ejecta coupled with strong radio emission. The pre-maximum spectra of the two objects show the presence of helium, leading Margutti et al. (2014) to suggest that the jet might have failed because it was damped by the additional helium layer in the progenitor. These objects appear to act as a bridge between the highly relativistic, collimated GRBs and more normal Type Ic SNe.

SN 2014ad was discovered on 2014 March 12.4 by the Catalina Real-Time Transient Survey, in PGC 37625 (Mrk 1309) at RA 11^{h}57^{m}44^s.44, Dec. −10°10′15″.7 (Howerton et al. 2014). The object was located 3.5 arcsec west and 7.2 arcsec north of the centre of the host galaxy. Howerton et al. (2014) reported that the early spectrum taken on March 14.9 and 15.9 with the South African Large Telescope showed a blue continuum and broad lines with minima near 4400 and 5100 Å. It was suggested that this object could be a peculiar Type Ia SN, either a Type Iax event or similar to SN 2002bj and SN 2005ek, or perhaps something unique (Howerton et al. 2014). Further spectroscopic observations of this object on March 16.9, 17.9 and 18.9 revealed the development of broad lines and its resemblance to broad-line Type Ic SNe like SN 1998bw and SN 2002ap, although with some differences in the line velocities and shapes. Recently, Stevance et al. (2017) presented a spectropolarimetric study of SN 2014ad. In this paper, we present the results of optical imaging and spectroscopy, together with the *Swift* Ultra Violet Optical Telescope (UVOT) data from the archives.

2 THE LIGHT-CURVE

2.1 Optical observations

Optical imaging of SN 2014ad was carried out in Bessell's *U*, *B*, *V*, *R* and *I* bands, using the Himalayan Faint Object Spectrograph Camera (HFOSC) mounted on the Himalayan Chandra Telescope (HCT). The photometric monitoring of this object started on 2014 March 13 (JD 245 6730.41), soon after discovery, and was continued until 2014 June 11 (JD 245 6820), when the object went into Solar conjunction. The central 2K × 2K region of the 2K × 4K pixel CCD chip was used for imaging observations. With a plate scale of 0.296 arcsec pixel^{-1}, the central 2K × 2K pixels cover a field of view of 10 × 10 arcmin^2. The gain and readout noise of the CCD camera are 1.22 electron ADU^{-1} and 4.87 electrons, respectively. Further details about the telescope and instrument can be obtained from http://www.iiap.res.in/centres/iao. On each night, several calibration frames, for example bias frames and twilight-sky flat frames, were taken. The observed data were reduced in a standard manner, using various tasks available within the Image Reduction and Analysis Facility (IRAF[1]) package.

Photometric standard regions PG1323-085, PG1525-071, PG1633+099 and PG2213-006 from the list of Landolt (1992) were observed on 2014 March 21, March 29, April 27, May 17 and June 4 under photometric sky conditions. Aperture photometry was performed to estimate the instrumental magnitudes of Landolt's standard stars. The aperture photometry was performed at two apertures, at an optimal aperture determined using the aperture growth curve and at an aperture close to full width at half-maximum (FWHM) of stellar profile. Bright stars in the field were used to determine an aperture correction between the two apertures. This correction was applied to the magnitude obtained at the smaller aperture. The average extinction coefficients for the site (Stalin et al. 2008) were used for atmospheric extinction correction. The average colour terms for the system were used to determine the photometric zero-points by fitting a linear relationship between the observed and standard colours. A sequence of secondary standards in the supernova field was calibrated using the estimated zero-points and average colour terms. Calibrated *UBVRI* magnitudes of the secondary standards, averaged over five nights, are given in Table 1 and have been marked

---

[1] IRAF is distributed by the National Optical Astronomy Observatories, which are operated by the Association of Universities for Research in Astronomy, Inc., under cooperative agreement with the National Science Foundation
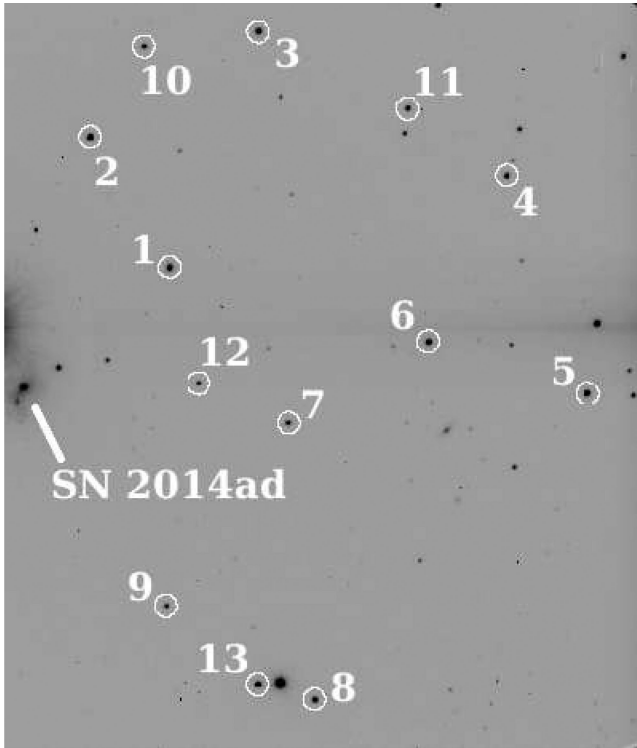
Figure 1. *R*-band image of SN 2014ad in the galaxy Mrk 1309. North is up and east to the left. The field stars marked with numbers 1–13 are used as local standards. The supernova is shifted close to the edge to avoid a nearby very bright star.

in Fig. 1. In order to avoid saturation owing to a very bright star next to the host galaxy, the supernova was placed close to the edge of the field of view.

The aperture- and profile-fitting photometry of the supernova suffer owing to the complex background of the host galaxy at the supernova location. Subtraction of the host galaxy image (template subtraction) works well in removing the galaxy background and results in accurate photometry. Deep template images of the host galaxy were obtained with the same instrumental setup, once the supernova faded sufficiently. The template images in the various bands were subtracted from the corresponding supernova frames, and aperture photometry was performed on the residual frames to estimate the instrumental magnitude of the supernova. The magnitudes of the secondary standards were measured using aperture photometry. Finally, the calibrated magnitudes of the supernova were obtained differentially with respect to the set of secondary standard stars in the supernova field. The supernova magnitudes in the *U*, *B*, *V*, *R* and *I* bands are listed in Table 2. The errors reported in Table 2 are estimated by taking into account the photometric error (computed by IRAF) and the calibration error.

2.2 *Swift* UVOT observations

The ground-based data on SN 2014ad were supplemented by data obtained by the UVOT onboard the *Swift* satellite and retrieved from the *Swift* data archive. SN 2014ad was observed from JD 245 6735 to JD 245 6754 in the optical broad-band filter *u* (3465 Å) and three UV filters, namely *uvw2* (1928 Å), *uvm2* (2246 Å) and *uvw1* (2600 Å). The data were reduced using various modules in HEASoft (the High Energy Astrophysics Software) following Poole et al. (2008) and

Brown et al. (2009). The magnitude of the supernova was obtained using the *uvotsource* task. This task performs aperture photometry at a user-defined aperture after taking into account the coincidence losses. Aperture photometry with an aperture of 5 arcsec is recommended. However, because the supernova was faint, photometry at a smaller aperture of 3 arcsec, having a high signal-to-noise ratio, was performed, and aperture correction provided by Poole et al. (2008) was applied to the extracted magnitudes. The background counts are estimated from the nearby region, using an aperture of size similar to that used for the supernova. *Swift* photometry of the supernova is reported in Table 3.

2.3 Light-curve evolution

The optical and UV light-curves of SN 2014ad are presented in Fig. 2. The optical observations started well before the phase of maximum light in the various bands, while the *Swift* UV observation covers only the first 20 d since *B* maximum. The light-curve evolution of SN 2014ad in the *B* band is similar to that in the *U* band and shows a fast decline soon after peak, whereas the *V*, *R* and *I* light-curves exhibit a slow decline. The *uvm*2 and *uvw*2 light-curves do not show any considerable evolution and they are almost flat. A similar flat behaviour was reported in the *uvw*1-band light-curve of SN 2009bb (Pignata et al. 2011), and was interpreted as resulting from the dominance of the background flux a few days after *B* maximum. In the absence of reference images in the *Swift* UV filters, a proper background subtraction is difficult.

The date of maximum light in the various bands is estimated by fitting a cubic spline to the observed data points around maximum light. The peaks in the bluer bands occur earlier than in the redder bands. The date of maximum and peak magnitude in the *U* band could not be determined, because we do not have enough pre-maximum data points. The peak in the *B* band occurred on JD 245 6735.11 $\pm$ 0.25, with an apparent magnitude of 14.787 $\pm$ 0.025 mag. The peak in the *V* band occurred at ~5.5 d, and the peak in the *R* and *I* bands occurred ~6.2 d after the *B*-band maximum.

SN 2014ad was discovered on 2014 March 12.40 (JD 245 6728.9) at an apparent magnitude of 15.7 mag. It was not detected in the image of the host galaxy obtained on March 06.37 (JD 245 6722.87), down to a limiting magnitude of 19.0 mag. Hence, date of explosion of SN 2014ad can be constrained as JD 245 6725 $\pm$ 3 d. Furthermore, the observed dates of maximum brightness indicate a rapid rise to maximum in the *B* band in 10 $\pm$ 3 d, and the *R*-band rise time as 16 $\pm$ 3 d.

The light-curve of SN 2014ad is plotted in Fig. 3 along with those of other well-studied Type Ic SNe, namely SN 1994I (Richmond et al. 1996), the broad-line Type Ic SN 2009bb (Pignata et al. 2011), SN 2007ru (Sahu et al. 2009), SN 2003jd (Valenti et al. 2008) and SN 2002ap (Foley et al. 2003; Pandey et al. 2003), and GRB 980425/SN 1998bw (Galama et al. 1998). The rising part of the light-curve of SN 2014ad is faster than that for SN 1998bw and similar to those of SN 2002ap and SN 2009bb. The light-curve decline in 15 d from the peak is estimated as $\Delta m_{15}(B) = 1.31 \pm 0.03$, $\Delta m_{15}(V) = 0.95 \pm 0.06$, $\Delta m_{15}(R) = 0.77 \pm 0.03$ and $\Delta m_{15}(I) = 0.62 \pm 0.02$.

The light-curve of SN 2014ad in all the bands is broader than that of Type Ic SN 1994I. Except for SN 1998bw, the post-maximum evolution of the light-curve of SN 2014ad is slower than that of the other SNe used for comparison. During the early post-maximum phase (<20 d after maximum in the *B* band) the *B*-, *V*- and *R*-band light-curves of SN 2014ad match well with those of SN 1998bw, and after that SN 2014ad declines faster than SN 1998bw.

Table 2. Optical *UBVRI* photometric observations of SN 2014ad with the Himalayan Chandra Telescope.

Date	JD[a]	Phase[b]	U	B	V	R	I
13/03/2014	730.407	−5	14.489 ± 0.010	15.237 ± 0.027	15.099 ± 0.013	14.934 ± 0.025	14.859 ± 0.028
14/03/2014	731.423	−4		15.065 ± 0.030	14.781 ± 0.015	14.697 ± 0.023	14.706 ± 0.027
18/03/2014	735.273	0	14.595 ± 0.020	14.705 ± 0.020	14.084 ± 0.061	13.992 ± 0.043	13.882 ± 0.082
19/03/2014	736.206	+1		14.756 ± 0.013	14.105 ± 0.020	13.908 ± 0.020	13.803 ± 0.019
21/03/2014	738.376	+3	14.985 ± 0.018	15.000 ± 0.009	14.003 ± 0.005	13.815 ± 0.019	13.733 ± 0.004
25/03/2014	742.316	+7	15.479 ± 0.015	15.257 ± 0.008	13.93 ± 0.006	13.771 ± 0.010	13.69 ± 0.006
26/03/2014	743.317	+8	15.572 ± 0.061	15.392 ± 0.010	13.960 ± 0.013	13.777 ± 0.006	13.716 ± 0.008
27/03/2014	744.250	+9	15.705 ± 0.029	15.669 ± 0.009	14.074 ± 0.012	13.815 ± 0.007	13.747 ± 0.013
28/03/2014	745.217	+10	15.919 ± 0.014	15.593 ± 0.006	14.064 ± 0.007	13.726 ± 0.014	13.769 ± 0.019
29/03/2014	746.212	+11	15.973 ± 0.019	15.784 ± 0.005	14.142 ± 0.011	13.866 ± 0.021	13.787 ± 0.011
30/03/2014	747.144	+12	16.133 ± 0.018	15.803 ± 0.014	14.202 ± 0.013	13.931 ± 0.009	13.832 ± 0.014
01/04/2014	749.385	+14	99.999 ± 0.999	15.989 ± 0.010	14.359 ± 0.011	14.048 ± 0.010	13.923 ± 0.012
03/04/2014	751.157	+16	16.515 ± 0.007	16.165 ± 0.006	14.489 ± 0.016	99.999 ± 0.999	14.024 ± 0.013
09/04/2014	757.151	+22	16.925 ± 0.007	16.628 ± 0.008	15.010 ± 0.010	14.593 ± 0.018	14.369 ± 0.009
11/04/2014	759.195	+24		16.616 ± 0.029	15.074 ± 0.060	14.710 ± 0.010	14.490 ± 0.013
14/04/2014	762.179	+27		16.748 ± 0.042	15.222 ± 0.019	14.901 ± 0.017	14.627 ± 0.016
17/04/2014	765.141	+30	17.039 ± 0.017	16.902 ± 0.019	15.407 ± 0.013	15.027 ± 0.018	14.771 ± 0.017
18/04/2014	766.094	+31		16.944 ± 0.010	15.580 ± 0.017	15.107 ± 0.020	14.819 ± 0.027
19/04/2014	767.128	+32		16.943 ± 0.012	15.481 ± 0.015	15.139 ± 0.022	14.843 ± 0.025
23/04/2014	771.104	+36	17.259 ± 0.018	17.019 ± 0.019	15.717 ± 0.019	15.308 ± 0.019	14.978 ± 0.022
27/04/2014	775.162	+40	17.523 ± 0.016	17.334 ± 0.027	15.918 ± 0.015	15.481 ± 0.022	15.106 ± 0.024
30/04/2014	778.113	+43	17.500 ± 0.014	17.199 ± 0.018	15.900 ± 0.018	15.509 ± 0.019	15.160 ± 0.021
03/05/2014	781.162	+46	17.611 ± 0.014	17.423 ± 0.014	15.936 ± 0.010	15.598 ± 0.010	15.226 ± 0.013
07/05/2014	785.108	+50	17.583 ± 0.023	17.340 ± 0.012	16.036 ± 0.031	15.685 ± 0.023	15.298 ± 0.025
14/05/2014	792.112	+57	17.784 ± 0.035	17.419 ± 0.016	16.241 ± 0.007	15.870 ± 0.012	15.489 ± 0.022
15/05/2014	793.135	+58	17.766 ± 0.054	17.389 ± 0.018	16.232 ± 0.010	15.894 ± 0.021	15.508 ± 0.012
17/05/2014	795.110	+60	17.718 ± 0.018	17.372 ± 0.010	16.323 ± 0.012	15.906 ± 0.013	15.538 ± 0.012
04/06/2014	813.130	+78	17.989 ± 0.038	17.540 ± 0.013	16.627 ± 0.010	16.300 ± 0.014	15.949 ± 0.006
11/06/2014	820.162	+85	17.937 ± 0.080	17.657 ± 0.026	16.861 ± 0.011	16.469 ± 0.021	16.005 ± 0.034

Notes. [a]245 6000+; [b]observed phase with respect to the epoch of *B*-band maximum: JD = 245 6735.11.

Table 3. UV/optical photometric observations of SN 2014ad with *Swift* UVOT.

Date	JD[a]	Phase[b]	uvw2	uvm2	uvw1	u
19/03/2014	735.69	0	17.667 ± 0.19	17.346 ± 0.13	16.010 ± 0.08	14.730 ± 0.04
21/03/2014	738.10	3	17.159 ± 0.14	17.154 ± 0.11	16.127 ± 0.08	14.971 ± 0.04
23/03/2014	740.36	5	17.233 ± 0.14	17.223 ± 0.08	16.467 ± 0.09	15.244 ± 0.04
25/03/2014	741.93	7	17.428 ± 0.18	17.515 ± 0.11	16.560 ± 0.10	15.651 ± 0.06
27/03/2014	743.96	9			16.653 ± 0.10	15.872 ± 0.16
29/03/2014	746.02	11	17.349 ± 0.16	17.608 ± 0.15	17.076 ± 0.14	16.074 ± 0.06
31/03/2014	747.91	13	17.183 ± 0.14	17.566 ± 0.17	17.062 ± 0.18	16.090 ± 0.11
03/04/2014	751.29	16	17.617 ± 0.17	17.591 ± 0.15	17.331 ± 0.20	16.293 ± 0.11
04/04/2014	751.63	16	18.037 ± 0.25	17.503 ± 0.13	17.182 ± 0.16	
06/04/2014	754.04	19	17.496 ± 0.13	17.369 ± 0.11	17.059 ± 0.12	16.529 ± 0.10

Notes. [a]245,6000+; [b]observed phase with respect to the epoch of *B* band maximum: JD = 245 6735.11.

The *I*-band light-curve of SN 2014ad is similar to those of SN 2007ru and SN 2003jd, and narrower than that of SN 1998bw. The *V*-band decline rate $\Delta m_{15}(V)$ of SN 2014ad is comparable to that of SN 2002ap, faster than that of SN 1998bw, and slower than those of SN 2003jd, SN 2007ru and SN 2009bb.

The dereddened colour curves of SN 2014ad are plotted in Fig. 4, along with those of SN 2009bb, SN 2007ru, SN 2003jd, SN 2002ap, SN 1998bw and SN 1994I. The colour curves of SN 2014ad have been corrected for colour excess $E(B - V) = 0.22$ mag (see Section 2.4), while the $E(B - V)$ values for other SNe were taken from their respective references. The $(B - V)$ colour evolution of SN 2014ad is similar to that of other broad-line Type Ic SNe, but different from the Type Ic supernova SN 1994I. The $(V - R)$ colour

evolution of SN 2014ad is similar to that of other broad-line Ic and Type Ic SNe. The $(R - I)$ colour of Type Ic SNe shows considerable dispersion, with SN 2014ad lying at the bluer end. The colour evolution of SN 2014ad is similar to that of SN 1998bw.

2.4 Reddening, distance and absolute magnitudes

The Galactic reddening in the direction of Mrk 1309, estimated from the infrared dust map of Schlegel, Finkbeiner & Davis (1998), is $E(B - V) = 0.045$ mag. The low-resolution spectrum of SN 2014ad around the epoch of maximum light shows a strong Na I D absorption line resulting from interstellar matter within the Milky Way, and a weaker absorption at the rest wavelength of the host galaxy.
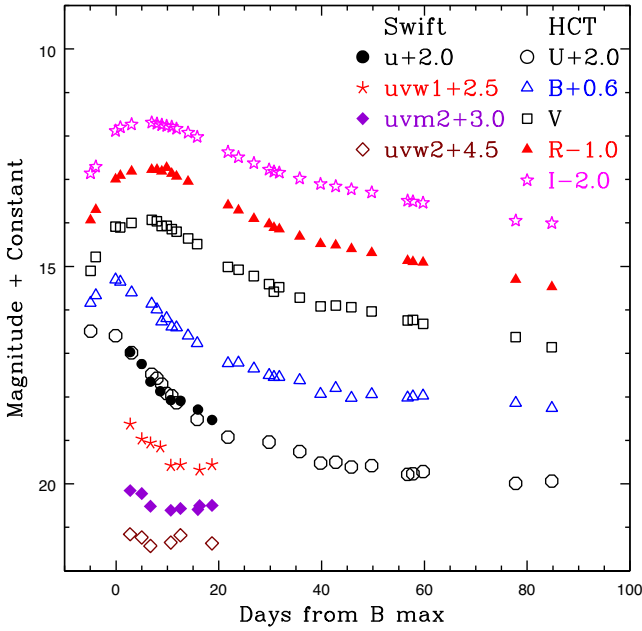
Figure 2. Optical *UBVRI* and *Swift* light-curves of SN 2014ad. The light-curves have been shifted by the amount indicated in the legend. The typical error in the photometry is less than the point size.
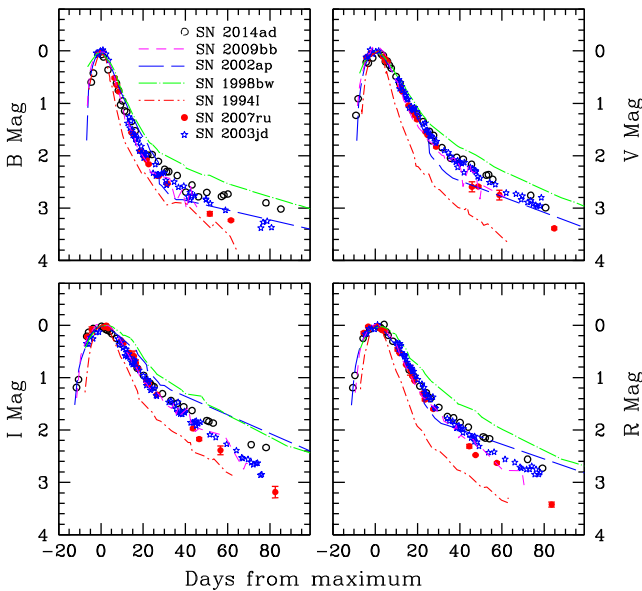
Figure 3. Light-curves of SN 2014ad compared with those of other well-studied broad-line and normal Ic SNe.

The five spectra of SN 2014ad, obtained close to maximum light, were averaged to improve the signal-to-noise ratio for measuring the equivalent width of the Na I D absorption line. The average equivalent width of the Galactic component of the Na I D line is 0.98 ± 0.06 Å and from the host galaxy is 0.06 ± 0.01 Å. Using the relationship between the equivalent width of the Na I D line and reddening (Poznanski, Prochaska & Bloom 2012), we estimate $E(B - V)_{\rm Gal} = 0.20 \pm 0.06$ mag, $E(B - V)_{\rm host} = 0.02$ mag and a total reddening of $E(B - V)_{\rm total} = 0.22 \pm 0.06$ mag. The estimated $E(B - V)_{\rm Gal}$ is high compared with the value reported by Schlegel et al. (1998). The estimated higher $E(B - V)_{\rm total}$ of SN 2014ad is consistent with
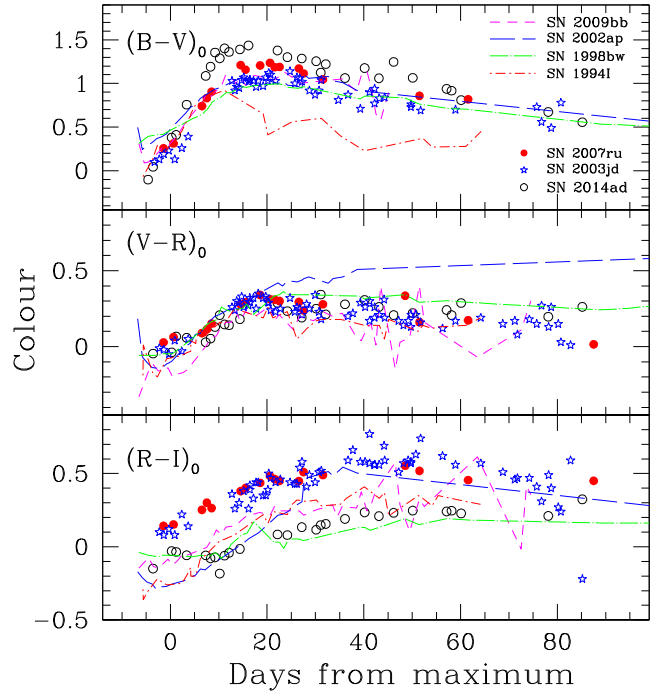
Figure 4. The colour curve evolution of SN 2014ad compared with that of other well-studied broad-line and normal Ic SNe.

colour evolution, and the reddening-corrected $(B - V)$ and $(V - R)$ colours of SN 2014ad are similar to those of other broad-line Type Ic SNe (see Fig. 4). For the analysis below, we adopt $E(B - V)_{\rm total} = 0.22 \pm 0.06$ mag.

The distance to the host galaxy Mrk 1309 of SN 2014ad was estimated using the radial velocity of the host, corrected for the Local Group infall onto the Virgo cluster, $V_{\rm Virgo} = 1904 \pm 32$ km s^{-1} (Mould et al. 2000). For $H_0 = 72$ km s^{-1} Mpc^{-1}, the distance to SN 2014ad is 26.44 Mpc and the distance modulus is 32.11 ± 0.15 mag.

The peak absolute magnitudes of SN 2014ad in the various bands have been estimated using the reddening and distance modulus referred to above. With a *V*-band absolute magnitude of -18.86 ± 0.23 mag, SN 2014ad is more luminous than Type Ic SNe 1994I ($M_V = -17.62 \pm 0.3$ mag; Richmond et al. 1996; Sauer et al. 2006), 2004aw ($M_V = -18.02 \pm 0.3$ mag; Taubenberger et al. 2006), 2007gr ($M_V = -17.22 \pm 0.18$ mag; Hunter et al. 2009), broad-line SNe 2012ap ($M_V = -18.67 \pm 0.08$ mag; Milisavljevic et al. 2015), 2009bb ($M_V = -18.65 \pm 0.34$ mag; Pignata et al. 2011), 2002ap ($M_V = -17.37 \pm 0.05$ mag; Foley et al. 2003; Pandey et al. 2003), and XRF 060218/SN 2006aj ($M_V = -18.67 \pm 0.08$ mag; Modjaz et al. 2006), and fainter than GRB 980425/SN 1998bw ($M_V = -19.12 \pm 0.05$ mag; Galama et al. 1998) and GRB 031203/SN 2003lw ($M_V = -19.75 \pm 0.5$ mag; Malesani et al. 2004). The *V*-band absolute magnitude of SN 2014ad is, however, comparable to those of broad-line SNe 2007ru ($M_V = -19.06 \pm 0.2$ mag; Sahu et al. 2009) and 2003jd ($M_V = -18.9 \pm 0.3$ mag; Valenti et al. 2008). Our estimate of M_V for SN 2014ad is consistent with that reported by Stevance et al. (2017).

The *R*-band absolute magnitude of SN 2014ad, namely -18.87 ± 0.3 mag, is comparable to those of broad-line Ic SNe ($M_R = -19.0 \pm 1.1$ mag) and engine-driven SNe ($M_R = -18.9 \pm 0.4$ mag), and brighter than normal Ic SNe ($M_R = -18.3 \pm 0.6$ mag) from the sample of Drout et al. (2011).

Table 4. Log of spectroscopic observations of SN 2014ad.

| Date	JD[a]	Phase[b]	Range (Å)
13/03/2014	730.35	−5	3500-7800; 5200-9250
14/03/2014	731.34	−4	3500-7800; 5200-9250
18/03/2014	735.31	0	3500-7800; 5200-9250
19/03/2014	736.22	+1	3500-7800; 5200-9250
21/03/2014	738.40	+3	3500-7800; 5200-9250
25/03/2014	742.34	+7	3500-7800; 5200-9250
27/03/2014	744.22	+9	3500-7800; 5200-9250
28/03/2014	745.37	+10	3500-7800; 5200-9250
29/03/2014	746.34	+11	3500-7800; 5200-9250
31/03/2014	748.12	+13	3500-7800; 5200-9250
04/04/2014	752.20	+17	3500-7800; 5200-9250
14/04/2014	762.13	+27	3500-7800; 5200-9250
16/04/2014	764.25	+29	3500-7800; 5200-9250
23/04/2014	771.30	+36	3500-7800; 5200-9250
27/04/2014	775.23	+40	3500-7800; 5200-9250
03/05/2014	781.14	+46	3500-7800; 5200-9250
17/05/2014	795.13	+60	3500-7800; 5200-9250
27/05/2014	805.19	+70	3500-7800; 5200-9250
04/06/2014	813.14	+78	3500-7800; 5200-9250
13/06/2014	822.17	+87	3500-7800; 5200-9250
22/02/2015[c]	1075.43	+340	4700-9000

Notes. [a]245,6000+; [b]in days relative to the *B*-band maximum; [c]observation taken with the Subaru Telescope.

3 THE OPTICAL SPECTRUM

3.1 Observations

Spectroscopic observations of SN 2014ad were performed from 2014 March 13 (JD 245 6730.35) to 2014 June 13 (JD 245 6822.17) using the HCT. In order to cover the entire optical waveband, the observations were carried out using grisms Gr#7 (wavelength range 3500–7800 Å) and Gr#8 (5200–9250 Å), available with the HFOSC. The spectral resolution is ∼7 Å. A late-phase spectrum was obtained with the 8.2-m Subaru Telescope equipped with the Faint Object Camera and Spectrograph (FOCAS; Kashikawa et al. 2002) on 2015 February 22. A 0.8-arcsec slit and B300 grism, covering 4700–9000 Å, were used for this observation. The journal of spectroscopic observations is given in Table 4. Spectroscopic data reduction was carried out using tasks available within IRAF. The spectra were bias-subtracted and flat-fielded. The one-dimensional spectra were extracted using the optimal extraction method. The one-dimensional spectra obtained with the HCT were wavelength-calibrated using the arc lamp spectra of FeAr and FeNe. The wavelength calibration for Subaru data was obtained using the ThAr arc lamp spectrum. The wavelength-calibrated spectra were cross-checked using bright night-sky emission lines, and, whenever required, a small shift was applied. The spectrum of spectrophotometric standard stars, observed on the same night, was used to correct for the instrumental response and to flux-calibrate the supernova spectra. The spectra in the two regions were combined, scaled to a weighted mean, to give the final spectrum on a relative flux scale. Except for the late-phase spectrum obtained using Subaru, spectra were brought to an absolute flux scale using the *UBVRI* magnitudes. The supernova spectra were corrected for the host galaxy redshift of $z = 0.01546$ (from NED) and dereddened by the total reddening $E(B − V)_{\text{total}} = 0.22$ mag as estimated in Section 2.4. The telluric lines have not been removed from the spectra.
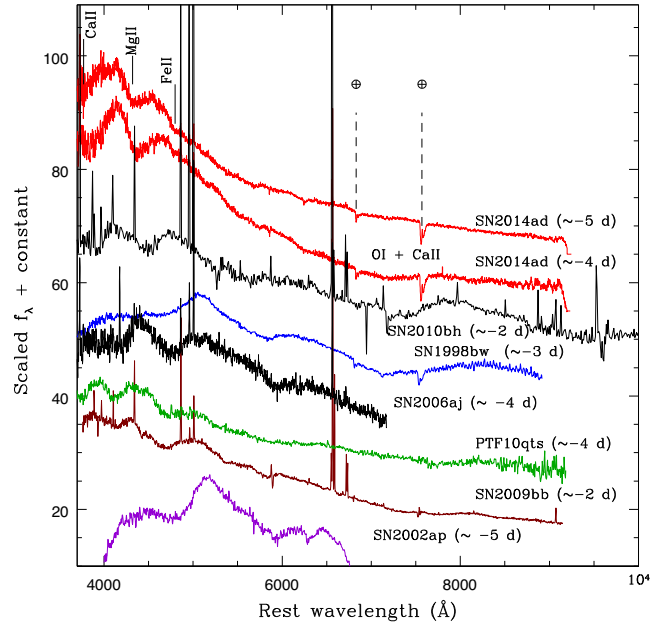
Figure 5. Pre-maximum spectra of SN 2014ad, compared with those of other broad-line Type Ic SNe at a similar epoch. For clarity, the spectra have been shifted vertically. Telluric lines are marked with a circled plus sign.

3.2 Spectral evolution

3.2.1 Pre-maximum spectral evolution

The spectral evolution of SN 2014ad in the pre-maximum phase is presented in Fig. 5. The first two spectra obtained on −5 and −4 d with respect to the *B*-band maximum show a blue continuum with two distinct broad absorptions at ∼3800 and ∼4400 Å. Weak notches are also seen at ∼4800 and ∼5800 Å in both spectra. The absorption at ∼3800 Å is caused by Ca II, and the absorptions at ∼4400 and ∼4800 Å are the result of Mg II and Fe II, respectively (Walker et al. 2014). In the −4-d spectrum, a depression is seen at ∼7300 Å that was not present in the spectrum taken on day −5. This feature is caused by the heavily blended O I and Ca II near-infrared (NIR) triplet, and requires the presence of sufficient material at velocities higher than 30 000 km s^{-1} (Mazzali et al. 2002). The apparent broad emission-like features at 4000 and 4600 Å in the early-phase spectra of SN 2014ad do not result from discrete emission lines, but are merely regions of low opacity, from where photons have a higher probability of escaping (Iwamoto et al. 1998; Mazzali, Iwamoto & Nomoto 2000).

The pre-maximum spectra of SN 2014ad is compared with the spectra of other broad-line Type Ic SNe 1998bw (Patat et al. 2001), PTF10qts (Walker et al. 2014), 2009bb (Pignata et al. 2011), 2010bh (Bufano et al. 2012) and 2002ap (Foley et al. 2003) obtained at a similar epoch, in Fig. 5. The shape of the spectrum of SN 2014ad is very similar to those of the spectra of PTF10qts, SN 2010bh and SN 2009bb; however, the features in the spectrum of SN 2014ad are blue-shifted to a greater extent. Except for SN 2002ap, all SNe show a blue continuum in the pre-maximum phase. There are noticeable differences between the spectrum of SN 2014ad and that of SN 1998bw: the spectrum of SN 1998bw does not show the pseudo-emission peak at ∼4400 Å seen in SN 2014ad, which is caused by the higher metal content at high velocity (Mazzali et al. 2013). The pseudo-emission peak at ∼6300 Å seen in the spectrum of SN 1998bw is absent in the spectrum of SN 2014ad, and the strong
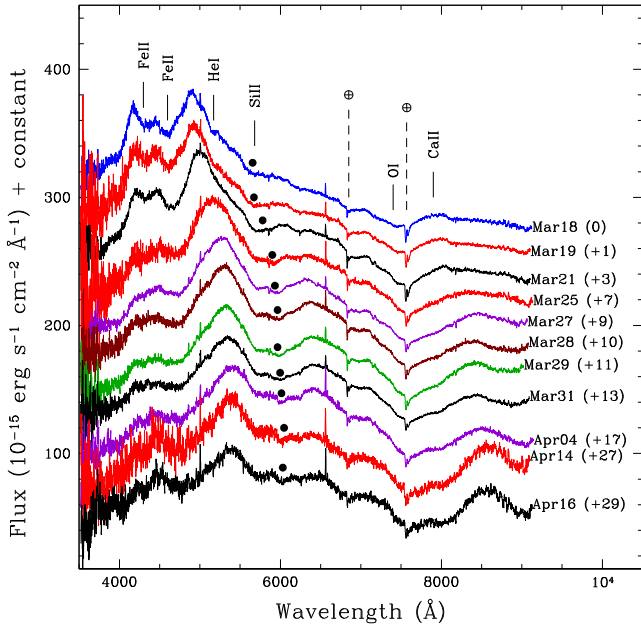
Figure 6. Spectral evolution of SN 2014ad during the early post-maximum phase. The black dots show the position of the Si II 6355 Å line. Telluric lines are marked with a circled plus sign.

Figure 7. Spectral evolution of SN 2014ad during the post-maximum phase. Telluric lines are marked with a circled plus sign.

absorption at ∼7300 Å is less pronounced in the spectrum of SN 2014ad. Features similar to those seen in SN 2014ad have also been noted in the pre-maximum spectra of GRB 130702A/SN 2013dx (D'Elia et al. 2015).

3.2.2 Spectral evolution during the maximum and post-maximum phase

The spectral evolution during the first month, when the light-curve shows a steep decline from maximum light, is shown in Fig. 6. The spectrum at the *B*-band maximum shows a significant evolution compared with the pre-maximum spectra. The continuum becomes redder, with emission peaks at ∼4200 and ∼4900 Å. The peak at ∼4200 Å weakens after the first few days, whereas the peak at ∼4900 Å remains, with a gradual redshift. A small number of broad features are seen in the spectrum and become increasingly dominant.

The main features in the spectra are caused by lines of Si II, O I, Ca II and Fe II. The weak notch seen in the pre-maximum spectra at ∼5800 Å appears to become stronger, which is probably a result of the Si II 6355-Å line. In the redder part of the spectrum, the O I line becomes stronger and is heavily blended with the Ca II NIR triplet.

The spectrum of SN 2014ad obtained close to maximum light shows a depression at ∼5200 Å. A similar feature was noticed in the spectrum of SN 2009bb and was associated with the He I 5876 Å line (Pignata et al. 2011). If this feature is indeed caused by the He I 5876-Å feature, it corresponds to a velocity of 37 000 km s⁻¹, which is consistent with the photospheric velocity deduced from the absorption trough of the Si II 6355-Å line (see Section 3.3). The broad absorption feature between 7300 and 8000 Å is similar to that seen in SN 2012ap and identified with multiple components of Ca II, including a detached component of high velocity and very high velocity (Milisavljevic et al. 2015).

The spectral evolution of SN 2014ad in the preiod +36 to +87 d is shown in Fig. 7. During this phase, the absorption-dominated
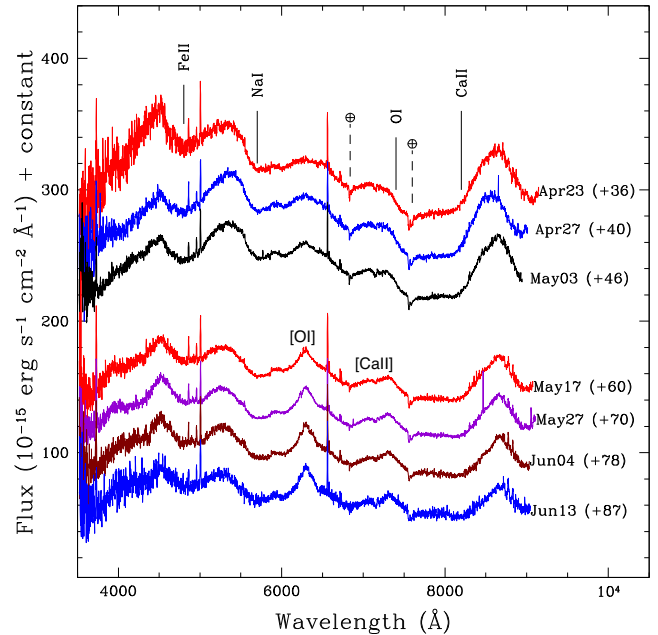
spectrum gradually changes to an emission-dominated spectrum, indicating the ongoing transition to the nebular phase. The blue part of the spectrum is increasingly suppressed, and the strength of the emission component of the Ca II NIR triplet increases. The absorption owing to the Na I D line becomes increasingly stronger. All the lines are still broad, indicating the persistence of the high expansion velocity of the ejecta.

The characteristic nebular lines resulting from [Mg I] 4571 Å, [O I] 6300, 6363 Å and [Ca II] 7291, 7324 Å, superimposed on the continuum, are seen in our spectrum obtained on +87 d. The presence of the continuum shows that the transition to the nebular phase is not yet complete.

The spectrum of SN 2014ad around maximum light is compared with the spectra of other broad-line objects obtained at a similar epoch in Fig. 8. With broad spectral features, the spectrum of SN 2014ad is very similar to those of SN 1998bw and SN 2010ah. A comparison of the +30-d spectrum of SN 2014ad with those of SN 1998bw, SN 2007ru and SN 2009bb shows that the spectra of all the SNe in the comparison look similar, except for the difference in the line broadening caused by differences in the expansion velocities (see Fig. 8). They are all dominated by the P-Cygni profile of the Ca II NIR triplet. The O I 7774-Å line in the spectra of SN 2014ad and SN 1998bw is weak; it is even weaker in SN 2007ru, but in SN 2009bb it is stronger compared with SN 2014ad.

3.2.3 Spectral evolution during the nebular phase

The spectrum of SN 2014ad obtained at +340 d is plotted in Fig. 9. This spectrum is dominated by [O I] 6300, 6363 Å and [Ca II] 7291, 7324 Å, possibly blended with [O II] 7320, 7330 Å forbidden emission lines. Narrow emission lines from the host galaxy are also prominent in this spectrum. Nebular spectra of SN 1998bw, SN 2002ap and SN 2012ap, around a similar epoch, have also been plotted for comparison.

The [O I] 6300, 6363 Å/[Ca II] 7291, 7324 Å emission line ratio is found to be 1.54. This line ratio is important as it can be used as a
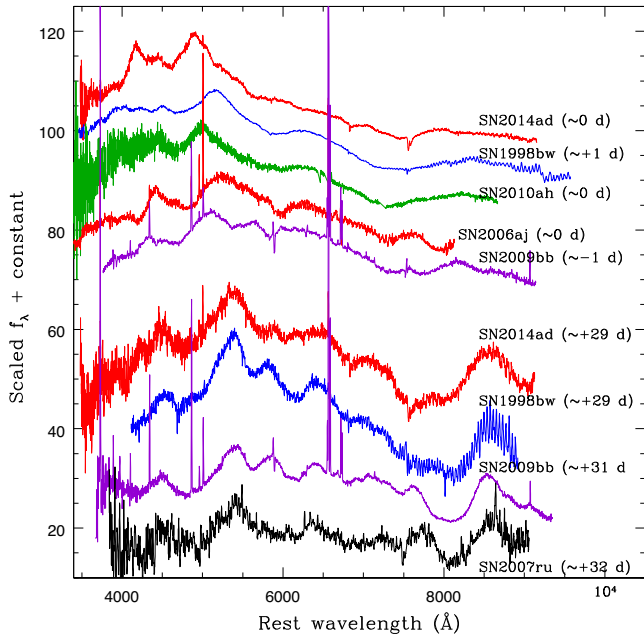
Figure 8. Spectra of SN 2014ad at *B*-band maximum and ∼1 month after maximum, compared with spectra of other broad-line Type Ic SNe at a similar epoch. For clarity, the spectra have been shifted vertically.
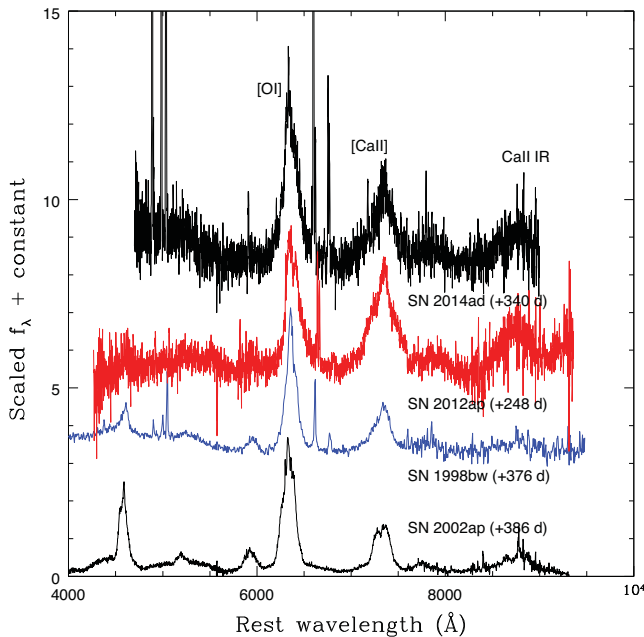
Figure 9. Nebular spectrum of SN 2014ad plotted with those of SN 1998bw, SN2002ap and SN 2012ap. For clarity, the spectra have been shifted vertically.

good diagnostic of the main sequence mass (M_{MS}) of the progenitor star (Maeda et al. 2007). The mass of O in the ejecta of core-collapse SNe is very sensitive to the M_{MS} of the progenitor and it increases with M_{MS}, whereas the mass of the explosively synthesized Ca is insensitive to the M_{MS} of the progenitor, making the [O I]/[Ca II] line ratio higher for massive progenitor stars (Nomoto et al. 2006). Kuncarayakti et al. (2015) compiled the [O I]/[Ca II] line ratio for several core-collapse SNe of similar age during the nebular phase. The line ratio is <1 for Type IIP SNe included in their plot. For
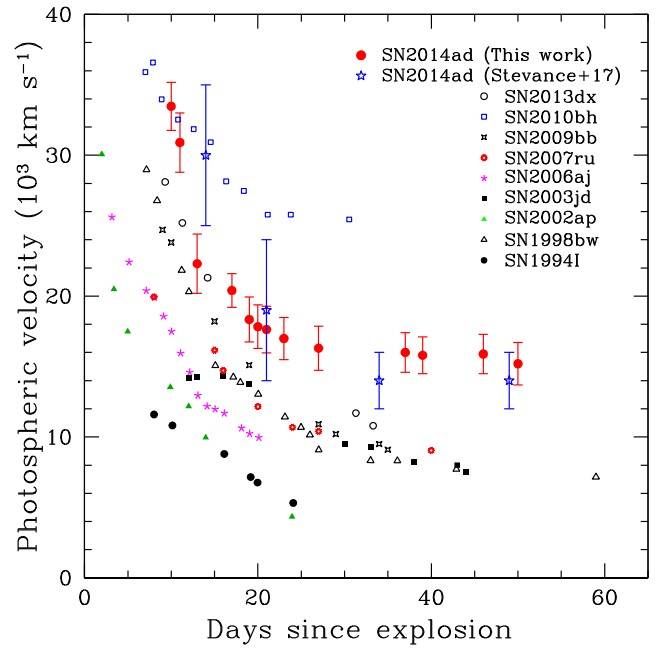
Figure 10. Temporal evolution of the photospheric velocity of SN 2014ad. The photospheric velocity measured by Stevance et al. (2017) is also shown. The Si II line velocities of other Type Ic SNe are also plotted for comparison.

stripped-envelope core-collapse SNe, Kuncarayakti et al. (2015) found that, depending on whether the progenitor star is in a binary system or is a single star, the ratio is different. The [O I]/[Ca II] line ratio for SN 2014ad (1.54) is comparable to those of SN 1998bw (1.7), SN 2002ap (2) and SN 2007ru (1.6), and higher than those of SN 2009bb (0.8) and SN 2012ap (0.9). A higher value of [O I]/[Ca II] for SN 2014ad indicates a higher M_{MS} for the progenitor star.

3.3 Photospheric velocity

In Type Ibc SNe, the expansion velocity estimated using the Fe II lines around 5000 Å is treated as representative of the photospheric velocity, as the other lines are formed far above the photosphere. The high expansion velocity of the ejecta in broad-line Ic SNe results in the blending of Fe II lines, making their identification difficult. In such cases, the expansion velocity measured using the Si II line is generally used as the photospheric velocity.

The photospheric velocity of SN 2014ad is measured using the absorption trough of the Si II 6355-Å line, in the redshift-corrected spectra. During the pre-maximum phase, owing to the severe blending of the spectral lines, identification of even the Si II feature is difficult. Hence, the velocity during the pre-maximum phase could not be measured. The position of the Si II feature is marked in the spectra shown in Fig. 6, and the temporal evolution of photospheric velocity is plotted in Fig. 10. The photospheric velocity of SN 2014ad, estimated by fitting the Fe II blend using SYN++ (Stevance et al. 2017), is also plotted in Fig. 10. Our photospheric velocity is consistent with estimates by Stevance et al. (2017). The Si II line velocity ranges from ∼33 500 km s^{-1} at *B* maximum to ∼15 000 km s^{-1} at about 40 d after *B* maximum. The Si II line velocity of SN 2014ad shows a steep decline from ∼33 500 to ∼21 000 km s^{-1} during the period ∼10 to 15 d after the explosion. A similar decrease in the expansion velocity during the first 20 d after the explosion has previously been noticed in other broad-line Type Ic SNe.
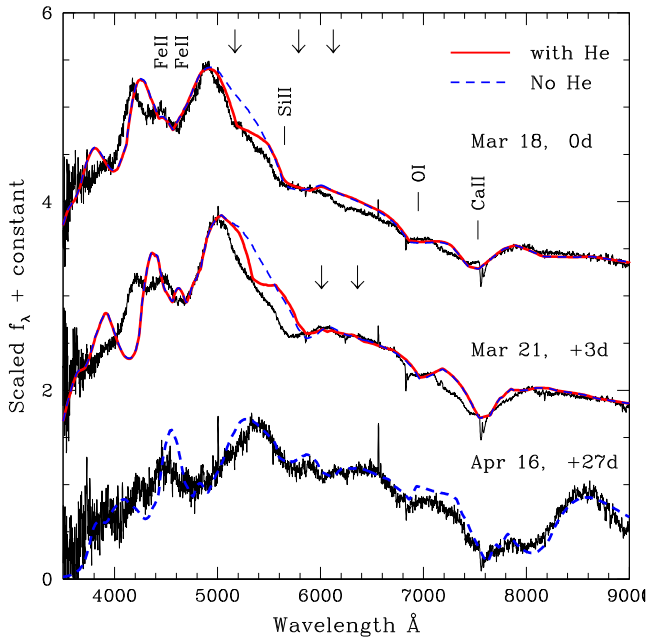
Figure 11. Spectra of SN 2014ad at 0 d, +3 d and +27 d, plotted with the synthetic fits generated using SYN++. The inclusion of He I improves the fit at ∼5400 Å. The expected position of the He I lines 5876, 6678 and 7065 Å are shown with arrows.

The photospheric velocities of other supernovae have also been plotted in Fig. 10 for comparison. We find that the velocity of ejecta in SN 2014ad is unusually high. Except for SN 2010bh, the expansion velocity of SN 2014ad is higher than those of all supernovae used in comparison. Beyond ∼20 d after explosion, the expansion velocity of SN 2014ad flattens at ∼15 000 km s^{-1}, while it flattens at ∼25 000 km s^{-1} for SN 2010bh, and at ∼8000 km s^{-1} for the other SNe.

3.4 Spectral fitting with SYN++

We used the SYN++ code, an enhanced version of the parametrized supernova spectrum synthesis code SYNOW (Fisher 2000), to generate synthetic spectra for SN 2014ad. The observed spectrum of SN 2014ad at maximum light is fitted well with a synthetic spectrum having a photospheric velocity of 35 000 km s^{-1} and a black-body temperature of 13 000 K (see Fig. 11). The synthetic spectrum includes ions of O I, Mg II, Si II, Ca II, Fe II and Co II. An excitation temperature of 6000 K was used for all the ions. The desired strengths of the lines were obtained by varying the optical depth, which is an exponential function of velocity. It can be seen that the synthetic spectrum with the above species does not fit the observed spectrum properly in the region 5000–5600 Å (shown by the dashed blue line), especially for the weak absorption around 5200 Å. This absorption minimum can be reproduced by introducing He I, marginally detached from the photosphere (shown by the solid red line), at a velocity of ∼40 000 km s^{-1}. The expected locations of other He I lines, 6678 and 7065 Å, are also marked in the spectrum. However, because these lines are usually fainter than the 5876-Å line, it is difficult to detect them. The observed flux in the spectrum of SN 2014ad in the region bluer than 4000 Å is drastically reduced. Such a flux deficit in the synthetic spectrum could not be produced by Co II/Fe II ions, but adding Fe I improves the fit.

The best fit to the spectrum of SN 2014ad at +3 d is obtained at a photospheric velocity of 25 000 km s^{-1} and a blackbody temper-

ature of 10 000 K. The ions included in the synthetic spectrum are the same as those used to fit the maximum-light spectrum with the same excitation temperature. Similar to the case of the maximum-light spectrum, the fit was examined with and without adding He I. The synthetic spectrum without He I appears to match the observed spectrum well. This is consistent with the finding of Stevance et al. (2017), who did not find any indication of helium in the spectrum obtained at +4 d. An additional high-velocity component of Ca II was included at 50 000 km s^{-1} to produce the broad feature of the Ca II NIR triplet.

The spectrum of SN 2014ad at +27 d has a good match to the synthetic spectrum having a photospheric velocity of 16 000 km s^{-1} and a blackbody temperature of 7000 K. The ions of O I, Na I, Si II, Ca II, Fe I, Fe II and Co II are included at an excitation temperature of 6000 K each. The broad and deep absorption feature of the Ca II NIR triplet is reproduced by adding an additional high-velocity component at 36 000 km s^{-1}.

The presence of the He I line in the spectra of the Type Ic event SN 1994I was explored by Filippenko et al. (1995) and Clocchiatti et al. (1996), and its possible contamination with other species, for example Na I, C I, was discussed by Millard et al. (1999) and Sauer et al. (2006). The detection of He I has been reported in the broad-line Type Ic SNe 2009bb (Pignata et al. 2011) and in 2012ap (Milisavljevic et al. 2015). The presence of He I in SN 2009bb is inferred through a comparison of the optical spectra with the synthetic spectra; the inclusion of helium in the synthetic spectrum is found to give a better fit to the observed spectrum. For SN 2012ap, the detection of He I in the optical spectra is supported by the presence of the 10 830- and 20 581-Å lines. The spectrum of SN 2010bh showed weak absorption features in the optical and NIR, compatible with He I 5876- and 10 830-Å lines. However, the presence of He I in SN 2010bh could not be confirmed because the 20 581-Å line could not be clearly identified (Bufano et al. 2012). We have shown that the inclusion of He I in the synthetic spectrum close to *B*-band maximum improves the fit marginally. An unambiguous detection of helium can be made only with NIR spectra and detailed spectral modelling.

3.5 Metallicity of the host galaxy in the supernova region

In order to understand the properties of the underlying region of the host galaxy, a spectrum of the supernova region was obtained on 2015 February 2, with the same settings as used for supernova observations. Narrow emission lines for hydrogen, oxygen and sulphur from the host galaxy are clearly seen in the spectrum. The emission-line fluxes were used to estimate the metallicity in the supernova region using various metallicity diagnostics available in the literature, such as the calibration by McGaugh (1991) and the *N*2 and *O*3*N*2 prescription of Pettini & Pagel (2004). The McGaugh calibration, which uses the R_{23} ratio, gives an oxygen abundance of 12 + log (O/H) = 8.38. The oxygen abundance estimated using the *N*2 and *O*3*N*2 index of Pettini & Pagel (2004) is 8.42 and 8.37, respectively. The oxygen abundance was also estimated using the host galaxy emission lines in the nebular spectrum of SN 2014ad, obtained with the Subaru telescope. It was found to agree well with the other estimates. The average value of 12 + log (O/H) = 8.4 ± 0.2 corresponds to ∼0.5 Z⊙. This shows that the metallicity in the supernova region is subsolar. Modjaz et al. (2008) have shown that GRBs are found in metal-poor environments compared with broad-line Type Ic SNe without GRBs. It is also shown that, following the strong line diagnostics of Kewley & Dopita (2002), the oxygen abundance of 12 + log (O/H) at the location of
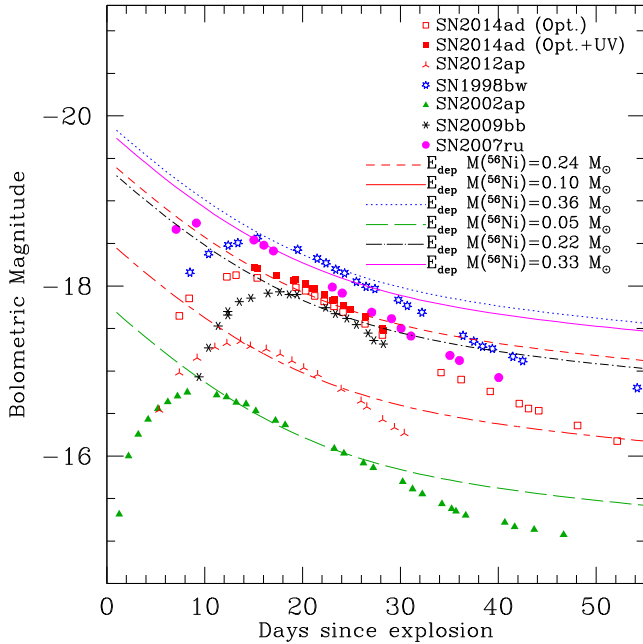
Figure 12. The quasi-bolometric light-curve of SN 2014ad and those of other broad-line Type Ic SNe. The overplotted lines correspond to the rate of energy production via the ^{56}Ni $\rightarrow$ ^{56}Co chain for various values of the mass of ^{56}Ni.

broad-line SNe Ic is ∼8.5, which corresponds to 0.2–0.6 Z$_\odot$, depending on the adopted metallicity scale and solar abundance value. Our estimates of metallicity at the location of SN 2014ad are consistent with the findings of Stevance et al. (2017) and Modjaz et al. (2008).

4 BOLOMETRIC LIGHT-CURVE

The quasi-bolometric light-curve of SN 2014ad was constructed using the optical and *Swift* UV magnitudes reported in Section 3. The observed magnitudes were corrected for a total extinction of $E(B − V) = 0.22$ mag, using the Galactic reddening law of Cardelli, Clayton & Mathis (1989). The extinction-corrected magnitudes were then converted to monochromatic flux at the filter effective wavelength, using the magnitude-to-flux conversion zero-points from Bessell, Castelli & Plez (1998). The fluxes were then interpolated using the spline function and integrated from 0.31 to 0.93 μm. The quasi-bolometric luminosity thus obtained is used to estimate the bolometric magnitude and is plotted in Fig. 12. During JD 245 6738 to JD 245 6751, when *Swift* UV data were available, the integration was carried out from 0.16 to 0.93 μm. The bolometric light-curve of SN 2014ad peaked on JD 245 6738 with bolometric magnitude −18.10 mag. The quasi-bolometric light-curves of some broad-line Type Ic SNe with and without GRBs, estimated in a similar way, are also plotted in the figure. The early post-maximum decline Δm_{15} of the quasi-bolometric light-curve of SN 2014ad is slower (Δm_{15}(Bol) = 0.80) than those of SNe 2009bb and 2012ap, and it is faster than those of SNe 1998bw and 2002ap. The late-phase (between +30 d and the last available data point) decline rate of SN 2014ad is 2.1 mag (100d)$^{-1}$, which is marginally faster than that of SN 1998bw but slower than that of SN 2009bb. The slower decline during the late phase indicates that the ejecta is still too thick for γ-rays to escape. Furthermore, in spite of the extremely high expansion velocity during the early phase and the relatively

high velocity (∼15 000 km s^{-1}) during the late phase, the slowly declining bolometric light-curve (indicative of the efficient trapping of γ-rays) of SN 2014ad hints at a massive ejecta.

An estimate of the contribution of UV (*uvm*2 and *uvw*2) bands to the bolometric luminosity is made. The first available *Swift* UV data point corresponds to ∼3 d after maximum in the *B* band. At this epoch, the UV flux contributes ∼10 per cent to the bolometric flux. The UV contribution decreases to ∼7 per cent at ∼15 d after *B* maximum. Thus, the contribution of the UV band is small even if the *uvw*2/*uvm*2 brightness is overestimated as a result of contamination by background light. There are only a few broad-line Type Ic SNe for which UV observations are available, and again the temporal coverage for most of them is sparse. For SN 2006aj, however, the contribution of the UV flux to the bolometric flux has been derived by Campana et al. (2006) and Cano et al. (2011). They showed that, because of the shock breakout of the progenitor star, during the first few days (∼2 d) after the explosion the contribution of the UV flux to the bolometric flux was high, and thereafter decayed rapidly. For SN 2014ad, the estimated UV contribution of ∼10 per cent to the bolometric flux at +3 d is consistent with the fraction estimated for SN 2006aj at a similar epoch. In the quasi-bolometric curve presented in Fig. 12, no correction has been applied for the missing flux in the IR bands. It has been shown that the missing flux in the NIR bands can contribute ∼20–25 per cent to the bolometric flux near maximum brightness, which increases to ∼40–50 per cent 1 month later (Tomita et al. 2006; Valenti et al. 2008; Cano et al. 2011). After including a contribution of 20 per cent for the missing band in the NIR, the peak bolometric magnitude of SN 2014ad is −18.32 mag.

5 EXPLOSION PARAMETERS

The bolometric light-curve derived in Section 4, along with information about the photospheric velocity, is used to estimate the explosion parameters, namely the mass of ejecta (M_{ej}), the kinetic energy (E_{k}) and the mass of ^{56}Ni synthesized in the explosion of SN 2014ad. The explosion parameters can be derived either by detailed hydrodynamical light-curve and spectral modelling of these events (Iwamoto et al. 1998; Mazzali et al. 2003, 2006; Valenti et al. 2008), by fitting the analytical model of Arnett (1982) to the estimated bolometric light-curve of the supernova, or by using the analytical formula for the total rate of energy production via ^{56}Ni $\rightarrow$ ^{56}Co (Nadyozhin 1994).

The energy production curves for different values of the mass of ^{56}Ni have been estimated and are plotted in Fig. 12 (thin lines), along with the quasi-bolometric light-curves. From the figure it is evident that the energy production rate for 0.24 M$_\odot$ of ^{56}Ni best matches the quasi-bolometric light-curve of SN 2014ad. For comparison, bolometric light-curves and the best-matching energy production curves corresponding to different values of ^{56}Ni for some other well-studied broad-line Ic SNe are also shown in Fig. 12, which are in good agreement with the values reported in the literature.

Alternatively, the mass of ^{56}Ni synthesized in the explosion can be estimated using Arnett's formulation (1982). This formulation is applicable to SNe for which the light-curves are powered purely by radioactive decay. The model assumes that, during the photospheric phase, the supernova ejecta expands homologously with spherical symmetry, ^{56}Ni is located at the centre without any mixing to outer layers, there is a single opacity over the duration of the explosion, and the ejecta is dominated by radiation pressure. The expression for the luminosity as a function of time, modified by Valenti et al.
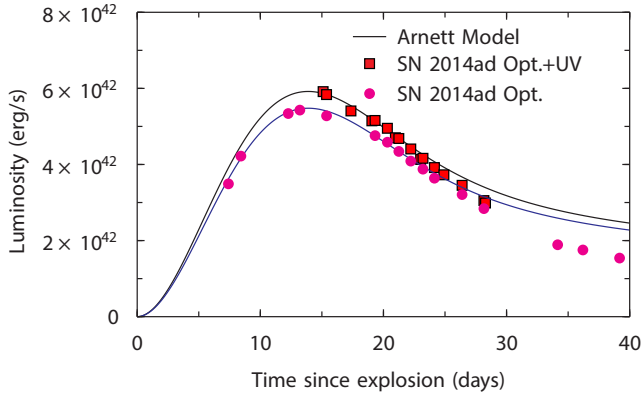
Figure 13. Arnett's analytical model fit to the quasi-bolometric light-curve of SN 2014ad.

(2008) to incorporate the energy produced by the decay of cobalt into iron, is used. The mass of ^{56}Ni and τ_m, the effective diffusion time that determines the overall width of the bolometric light curve, are the only free parameters in the expression for the luminosity. For a uniform density, the ejecta kinetic energy E_k and the effective diffusion time-scale τ_m (Arnett 1982, 1996) are given by

$$E_k \approx \frac{3}{5} \frac{M_{ej} v_{ph}^2}{2}, \tag{1}$$

$$\tau_m = \left(\frac{\kappa}{\beta c}\right)^{1/2} \left(\frac{6 M_{ej}^3}{5 E_k}\right)^{1/4}, \tag{2}$$

where, κ is the optical opacity, taken as 0.07 cm^{2}g^{-1} (Chugai 2000), $\beta \approx 13.8$ is a constant of integration (Arnett 1982) and c is the speed of light.

The quasi-bolometric light-curve of SN 2014ad is fitted with the modified Arnett's formulation by varying the mass of ^{56}Ni and τ_m. This formulation assumes that the material is in the photospheric phase, which is valid until $\sim$30 d, and hence the bolometric light curve until 30 d was considered for fitting Arnett's model. The best model fit to the quasi-bolometric light-curve is shown in Fig. 13. For the *UBVRI* quasi-bolometric light-curve, the best-fitting values of τ_m and mass of ^{56}Ni are 11.6 $\pm$ 0.6 d and 0.22 M$_\odot$, respectively. The inclusion of the *Swift* UV contribution to the quasi-bolometric light-curve increases the mass of ^{56}Ni to $\sim$0.24 M$_\odot$. The mass of ^{56}Ni derived using the energy deposition curve and that using Arnett's formulation are in good agreement.

The photospheric velocity, at the time of bolometric maximum (13 d after explosion), is measured as $v_{ph} = 22\,300 \pm 2100$ km s^{-1}. The mass of ejecta estimated in this way is $M_{ej} = 3.3 \pm 0.8$ M$_\odot$, and the kinetic energy of explosion $E_k = (1 \pm 0.3) \times 10^{52}$ erg. The errors in the explosion parameters are estimated by taking into account the errors in τ_m and the measured photospheric velocity. The mass of ^{56}Ni and the ejecta mass for SN 2014ad matches well with the median value for broad-line Ic SNe; however, the kinetic energy is much higher than its median value for broad-line Ic SNe (0.6 $\times 10^{52}$ erg) estimated by Cano (2013). Drout et al. (2011) proposed an empirical relationship between the mass of ^{56}Ni synthesized in the explosion and the extinction-corrected *R*-band absolute magnitude of the SNe:

$$\log(M_{^{56}\mathrm{Ni}}/\mathrm{M}_\odot) = -0.41\,M_R - 8.3, \tag{3}$$

where $M_{^{56}\mathrm{Ni}}$ is the mass of ^{56}Ni and M_R is the extinction-corrected *R*-band absolute magnitude of the supernova. The extinction-corrected *R*-band absolute magnitude of SN 2014ad
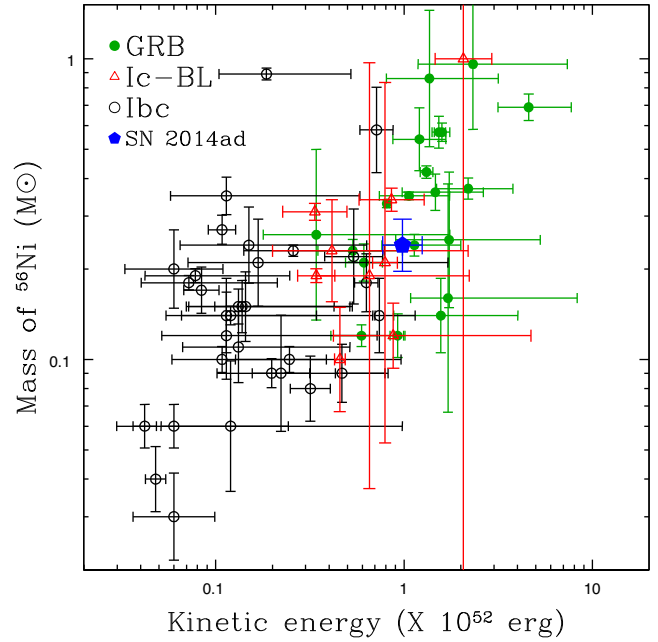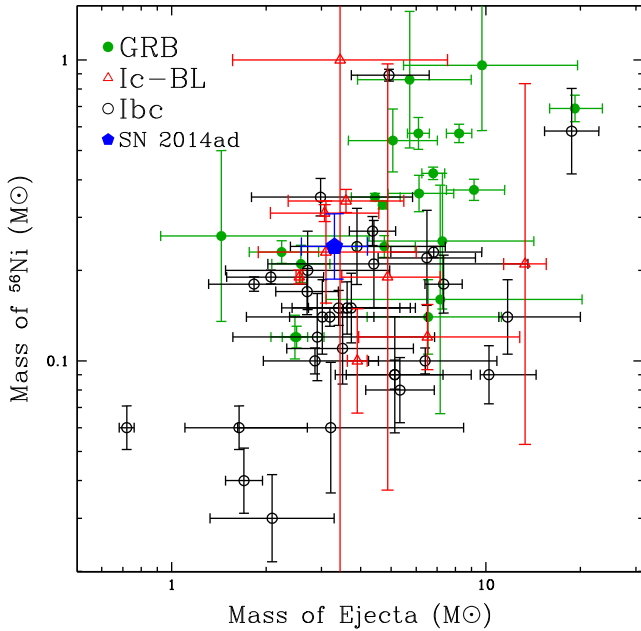

Figure 14. The mass of ^{56}Ni synthesized in the explosion versus the kinetic energy of explosion for GRB/XRF SNe, Type Ibc SNe and broad-line Type Ic SNe.

is $M_R = -18.87 \pm 0.30$ mag. This leads to a mass of ^{56}Ni of 0.27 $\pm$ 0.06 M$_\odot$, which is consistent with other estimates of the mass of ^{56}Ni.

Cano (2013) suggested yet another method for estimating the explosion parameters of Type Ibc SNe. In this method, the stretch and luminosity factors in the *BVRI* filter for a given supernova are determined relative to *k*-corrected light-curves of the template supernova SN 1998bw. The bolometric light-curve of SN 1998bw is then scaled with the average stretch and luminosity factors. The transformed bolometric light-curve is fitted with the analytical model of Arnett (1982), and the mass of ^{56}Ni, the mass of the ejecta and the kinetic energy of explosion are determined. The advantage of using this method lies in the fact that the explosion parameters can be determined for those objects for which data are sparse or not available in all of the optical bands. Using this method, Cano (2013) estimated the explosion parameters for a sample of GRB/XRF SNe, Type Ibc SNe and broad-line Type Ic SNe.

The explosion parameters from Cano (2013) are plotted in Figs 14, 15 and 16. The parameters for SN 2014ad are also plotted in the same figures to check the position of SN 2014ad in these diagrams. It was pointed out by Toy et al. (2016) that there was a typo in the expression for E_k in Arnett (1982), which was later corrected in Arnett (1996). The expression used for estimating E_k and M$_{ej}$ in this work takes this into account. Because the kinetic energy E_k was estimated by Cano (2013) using $E_k = M_{ej} v_{ph}^2 / 2$, their reported values of E_k have been scaled by a factor of 3/5 to enable comparison with this work.

From Fig. 14, a correlation between the mass of ^{56}Ni synthesized in the explosion and the kinetic energy of explosion E_k is evident: objects with higher kinetic energy tend to produce more ^{56}Ni in the explosion. The Type Ibc SNe are the explosions with lower kinetic energy, and the mass of ^{56}Ni produced in them is also on the lower side; broad-line Type Ic SNe exhibit higher kinetic energy and produce relatively larger amounts of ^{56}Ni. As expected, the GRB/XRF SNe are associated with extremely high kinetic energy

Figure 15. The mass of ^{56}Ni synthesized in the explosion versus the mass of ejecta for GRB/XRF SNe, Type Ibc SNe and broad-line Type Ic SNe.
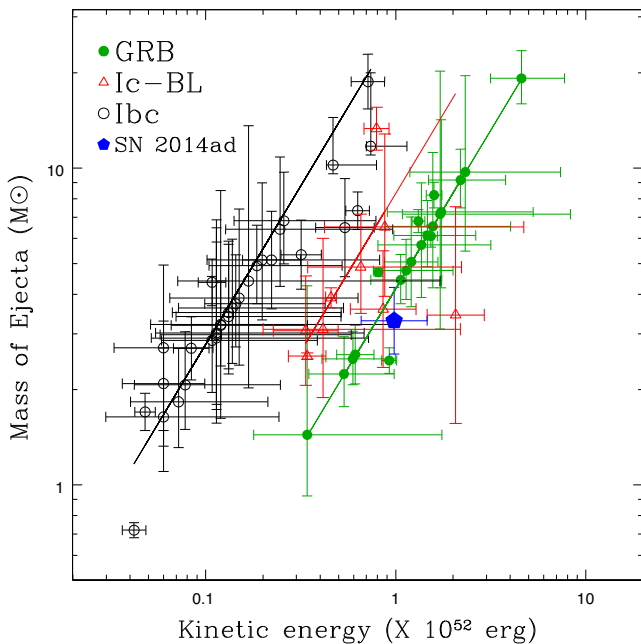
Figure 16. The mass of ejecta versus the kinetic energy of explosion for GRBs, Type Ibc and broad-line Type Ic SNe. The solid lines correspond to the median value of the E_k/M_{ej} ratio for Type Ibc, broad-line Ic SNe and GRBs.

and produce a large amount of ^{56}Ni. In the E_k–^{56}Ni plane, SN 2014ad appears closer to the GRB/XRF-associated SNe than to the broad-line Ic SNe. In Fig. 15, a correlation between the mass of ^{56}Ni and the mass of the ejecta is seen, although it is not as strong as seen in the plot between the mass of ^{56}Ni and the kinetic energy of explosion. In this plot, different subclasses of SNe do not occupy distinct regions and there is significant overlap.

In Fig. 16 two clear sequences are seen. There is a tight correlation between M_{ej} and E_k in the case of Type Ibc SNe. Similarly,
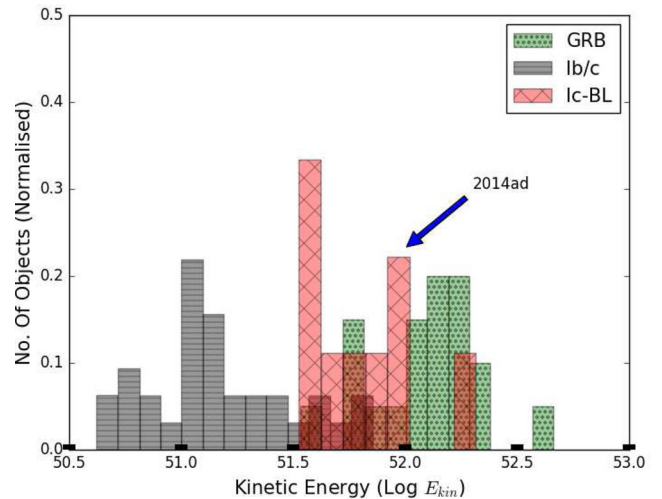
Figure 17. Distribution of Type Ibc, broad-line Type Ic SNe and GRBs as a function of kinetic energy.

GRB/XRF SNe also show a tight correlation, but with a shift towards higher E_k/M_{ej} ratios. Most of the broad-line Ic SNe are located in the region between the Ibc SNe and GRB/XRF-associated SNe. Lyman et al. (2016) provide similar plots in which they have included SNe IIb, Ib, Ic and broad-line Ic. The observed tight correlation between M_{ej} and E_k for SNe IIb, Ib and Ic was interpreted as the result of the similar photospheric velocity that they exhibit. Although broad-line Ic SNe have ejecta masses similar to those of SNe Ibc, because of their high expansion velocity they show a high E_k/M_{ej} ratio. With relatively higher kinetic energy and lower ejecta mass, SN 2014ad is located close to the strip occupied by GRB/XRF-associated SNe. In Fig. 17, using the data from Cano (2013), the distribution of Ibc, broad-line Ic SNe and GRBs as a function of kinetic energy is plotted. In this distribution, with kinetic energy $E_k = (1 \pm 0.3) \times 10^{52}$ ergs, SN 2014ad lies close to the region occupied by GRBs.

From the above discussion, it is clear that at bolometric peak the expansion velocity of the ejecta ($\sim$22 300 km s^{-1}) is high and the E_k/M_{ej} ratio ($\sim$0.30) of SN 2014ad is larger than all other well-studied broad-line Ic SNe (median value of E_k/M_{ej} ratio $\sim$0.12). In fact, the E_k/M_{ej} ratio for SN 2014ad is even higher than for GRB/XRF SNe (median value $\sim$0.24), except for SN 2010bh (GRB 100316D; Cano et al. 2011). We checked for the possible association of SN 2014ad with a GRB/XRF. There is no report of a detection of any GRB from 19 February 2014 near the supernova location. SN 2014ad was observed with the *Swift* X-ray Telescope (XRT; Burrows et al. 2005), but there is no report of the detection of this supernova in the X-ray either.

There are two other broad-line Type Ic SNe, namely SN 2009bb (Pignata et al. 2011) and SN 2012ap (Milisavljevic et al. 2015): both are bright in the radio and mildly relativistic; neither is associated with a GRB/XRF; and neither showed X-ray emission at late times. In both cases, helium was detected in the early-time optical spectra with photospheric velocities >20 000 km s^{-1}, during the nebular phase the emission line flux ratio [O I]/[Ca II] < 1, and the metallicity of the supernova location is solar to super-solar. The explosion properties of both of these objects were shown to fall between those of normal Ibc events and those of SNe associated with GRBs. They were proposed to be weak engine-driven explosions, where the engine activity stops before being able to produce a successful jet breakout (Margutti et al. 2014). Because the jet is not able to pierce through the stellar envelope, only a small fraction of energy

is dissipated at γ-ray frequencies, resulting in their non-detection in the γ-ray region.

The factors that might differentiate between broad-line Ic SNe without GRB and GRB-associated SNe are the different lifetimes of the central engine and progenitor properties (Margutti et al. 2014). The short-lived engine may not be able to power the jets sufficiently to enable them to pierce through the envelope of the progenitor to produce a GRB; and will result as relativistic SNe (Lazzati et al. 2012). Most of the observed GRBs are associated with a metal-poor environment (Modjaz et al. 2008). However, the discovery of GRBs in high-metallicity environments (Graham & Fruchter 2013) indicates that, although the metallicity has some role, it may not be the ultimate parameter deciding the final explosion outcome (Margutti et al. 2014). The presence of helium is the other factor that affects the breakout of the jet. The presence of helium in SN 2009bb and SN 2012ap is an indication that the helium layers in the progenitor of these events are not fully removed. Margutti et al. (2014) discussed the possibility that this helium layer may slow down the jet, which subsequently fails to break through the progenitor, resulting in relativistic SNe.

Some of the properties of SN 2014ad, namely no association with a GRB/XRF, high ejecta velocity, weak/no X-ray emission, are also found in SN 2009bb and SN 2012ap. The nebular line flux ratio and metallicity in the supernova region of SN 2014ad are higher than for SN 2009bb and SN 2012ap. In spite of the high kinetic energy and high E_k/M_{ej} ratio, no GRB was detected for SN 2014ad. One reason for the non-detection of a GRB associated with SN 2014ad may be that the jet points away from the line of sight of the observer. Other possibilities are that the central engine was weak and short-lived or that some mechanism, such as the presence of a thin helium layer, slowed down the jet, which then failed to break out through the progenitor.

For the very energetic broad-line Type Ic supernova SN 2010ah, the explosion parameters were estimated by Mazzali et al. (2013) using spectral and light-curve modelling. They inferred that SN 2010ah resulted from the explosion of a CO core of $\sim$5–6 $M_\odot$ and that the zero-age main sequence mass (M_{MS}) of the progenitor star was 24–28 $M_\odot$. Our estimates of the explosion parameters for SN 2014ad are similar to those for SN 2010ah, indicating that the progenitor for SN 2014ad may also be a massive one. If we assume that a neutron star of $\sim$1.4–2.0 $M_\odot$ is formed, the CO core mass is $\sim$3.9–6.1 $M_\odot$. This mass range corresponds to a main sequence mass of $M_{MS} \sim$ 20–25 $M_\odot$, which is lower than for SN 2010ah. If we assume that a black hole more massive than $\sim$3 $M_\odot$ is formed, and that the mass of the CO core $\geq$ 6 $M_\odot$, then the $M_{MS} \geq$ 25 $M_\odot$. Our inference of a massive progenitor for SN 2014ad based on the nebular line ratio [O I]/[Ca II] is consistent with this.

6 SUMMARY

In this paper, results based on low-resolution optical spectroscopy, optical imaging and *Swift* UVOT imaging of the broad-line Type Ic supernova SN 2014ad have been presented. With an absolute *V*-band magnitude of -18.86 ± 0.23 mag, this object is brighter than normal, and most broad-line Type Ic SNe, but fainter than GRB-associated SNe. The width of the spectral features and the expansion velocity of the ejecta are found to be very high. In the early phase, the expansion velocity is as high as $0.1c$, and during the late phase the expansion velocity is also found to be higher than other objects of similar class, except for the GRB-associated SN 2010bh. The explosion parameters determined by fitting Arnett's formulation to the derived bolometric light-curve show it to be a highly energetic

explosion; however, no GRB/X-ray flash was found to be associated with it. The main sequence mass of the progenitor star is estimated to be $\geq$20 $M_\odot$.

REFERENCES

Arnett W. D., 1982, ApJ, 253, 785
Arnett D., 1996, Supernovae and Nucleosynthesis: An Investigation of the History of Matter, from the Big Bang to the Present. Princeton Univ. Press, Princelton
Bessell M. S., Castelli F., Plez B., 1998, A&A, 333, 231
Brown P. J. et al., 2009, AJ, 137, 4517
Bufano F. et al., 2012, ApJ, 753, 67
Burrows D. N. et al., 2005, Space Sc. Rev., 120, 165
Campana S. et al., 2006, Nature, 442, 1008
Cano Z., 2013, MNRAS, 434, 1098
Cano Z. et al., 2011, ApJ, 740, 41
Cardelli J. A., Clayton G. C., Mathis J. S., 1989, ApJ, 345, 245
Chugai N. N., 2000, Astron. Lett., 26, 797
Clocchiatti A., Wheeler J. C., Brotherton M. S., Cochran A. L., Wills D., Barker E. S., Turatto M., 1996, ApJ, 462, 462
D'Elia V. et al., 2015, A&A, 577, A116
Drout M. R. et al., 2011, ApJ, 741, 97
Filippenko A. V., 1997, ARA&A, 35, 309
Filippenko A. V. et al., 1995, ApJ, 450, L11
Fisher A. K., 2000, PhD thesis, Univ. Oklahoma
Foley R. J. et al., 2003, PASP, 115, 1220
Galama T. J. et al., 1998, Nature, 395, 670
Graham J. F., Fruchter A. S., 2013, ApJ, 774, 119
Hjorth J. et al., 2003, Nature, 423, 847
Howerton S. et al., 2014, Cent. Bur. Electron. Telegram, 3831
Hunter D. J. et al., 2009, A&A, 508, 371
Iwamoto K. et al., 1998, Nature, 395, 672
Kashikawa N. et al., 2002, PASJ, 54, 819
Kewley L. J., Dopita M. A., 2002, ApJS, 142, 35
Kuncarayakti H. et al., 2015, A&A, 579, A95
Landolt A. U., 1992, AJ, 104, 340
Langer N., 2012, ARA&A, 50, 107
Lazzati D., Morsony B. J., Blackwell C. H., Begelman M. C., 2012, ApJ, 750, 68
Lyman J. D., Bersier D., James P. A., Mazzali P. A., Eldridge J. J., Fraser M., Pian E., 2016, MNRAS, 457, 328

Maeda K. et al., 2007, ApJ, 658, L5
Malesani D. et al., 2004, ApJ, 609, L5
Margutti R. et al., 2014, ApJ, 797, 107
Mazzali P. A., Iwamoto K., Nomoto K., 2000, ApJ, 545, 407
Mazzali P. A. et al., 2002, ApJ, 572, L61
Mazzali P. A. et al., 2003, ApJ, 599, L95
Mazzali P. A. et al., 2006, ApJ, 645, 1323
Mazzali P. A., Walker E. S., Pian E., Tanaka M., Corsi A., Hattori T., Gal-Yam A., 2013, MNRAS, 432, 2463
McGaugh S. S., 1991, ApJ, 380, 140
Milisavljevic D. et al., 2015, ApJ, 799, 51
Millard J. et al., 1999, ApJ, 527, 746
Modjaz M. et al., 2006, ApJ, 645, L21
Modjaz M. et al., 2008, AJ, 135, 1136
Modjaz M., Liu Y. Q., Bianco F. B., Graur O., 2016, ApJ, 832, 108
Mould J. R. et al., 2000, ApJ, 529, 786
Nadyozhin D. K., 1994, ApJS, 92, 527
Nomoto K., Tominaga N., Umeda H., Kobayashi C., Maeda K., 2006, Nucl. Phys. A, 777, 424
Pandey S. B., Anupama G. C., Sagar R., Bhattacharya D., Sahu D. K., Pandey J. C., 2003, MNRAS, 340, 375
Patat F. et al., 2001, ApJ, 555, 900
Perna R., Loeb A., 1998, ApJ, 509, L85
Pettini M., Pagel B. E. J., 2004, MNRAS, 348, L59
Pian E. et al., 2006, Nature, 442, 1011
Pignata G. et al., 2011, ApJ, 728, 14
Poole T. S. et al., 2008, MNRAS, 383, 627

Poznanski D., Prochaska J. X., Bloom J. S., 2012, MNRAS, 426, 1465
Rhoads J. E., 1999, ApJ, 525, 737
Richmond M. W. et al., 1996, AJ, 111, 327
Sahu D. K., Tanaka M., Anupama G. C., Gurugubelli U. K., Nomoto K., 2009, ApJ, 697, 676
Sanders N. E. et al., 2012, ApJ, 756, 184
Sauer D. N., Mazzali P. A., Deng J., Valenti S., Nomoto K., Filippenko A. V., 2006, MNRAS, 369, 1939
Schlegel D. J., Finkbeiner D. P., Davis M., 1998, ApJ, 500, 525
Shivvers I. et al., 2017, PASP, 129, 054201
Soderberg A. M., Nakar E., Berger E., Kulkarni S. R., 2006, ApJ, 638, 930
Stalin C. S., Hegde M., Sahu D. K., Parihar P. S., Anupama G. C., Bhatt B. C., Prabhu T. P., 2008, Bull. Astron. Soc. India, 36, 111
Stanek K. Z. et al., 2003, ApJ, 591, L17
Stevance H. F. et al., 2017, MNRAS, 469, 1897
Taubenberger S. et al., 2006, MNRAS, 371, 1459
Tomita H. et al., 2006, ApJ, 644, 400
Toy V. L. et al., 2016, ApJ, 818, 79
Turatto M., 2003, in Weiler K., ed., Lecture Notes in Physics, Vol. 598, Supernovae and Gamma-Ray Bursters. Springer-Verlag, Berlin, p. 21
Valenti S. et al., 2008, MNRAS, 383, 1485
Walker E. S. et al., 2014, MNRAS, 442, 2768
Waxman E., 2004, ApJ, 602, 886

This paper has been typeset from a T_EX/L^AT_EX file prepared by the author.